

Humic acid-induced formation of tobermorite upon hydrothermal treatment with municipal solid waste incineration bottom ash and its application for efficient removal of Cu(II) ions

Luo, Hongwei; He, Dongqin; Zhu, Weiping; Wu, Yichao; Chen, Zhitao; Yang, En-Hua

2019

Luo, H., He, D., Zhu, W., Wu, Y., Chen, Z., & Yang, E.-H. (2019). Humic acid-induced formation of tobermorite upon hydrothermal treatment with municipal solid waste incineration bottom ash and its application for efficient removal of Cu(II) ions. *Waste Management*, 84, 83-90. doi:10.1016/j.wasman.2018.11.037

<https://hdl.handle.net/10356/104247>

<https://doi.org/10.1016/j.wasman.2018.11.037>

© 2019 Elsevier. All rights reserved. This paper was published in *Waste Management* and is made available with permission of Elsevier.

Downloaded on 13 Mar 2024 16:57:14 SGT

1 **Humic acid-induced formation of tobermorite upon hydrothermal treatment with**
2 **municipal solid waste incineration bottom ash and its application for efficient removal of**
3 **Cu(II) ions**

4

5 Hongwei Luo^{a,b,†}, Dongqin He^{a,†}, Weiping Zhu^c, Yichao Wu^{c,d}, Zhitao Chen^c, En-Hua Yang^{c,*}

6

7 ^aCollege of Environment, Zhejiang University of Technology, Hangzhou, 310014, China

8 ^bEnergy Research Institute, Nanyang Technological University, Singapore 637553

9 ^cSchool of Civil and Environmental Engineering, Nanyang Technological University,
10 Singapore 639798

11 ^dCollege of Resources and Environment, Huazhong Agricultural University, Wuhan, 430070,
12 China

13

14 † These authors contributed equally to this work

15

16

17 *** Corresponding author:**

18 Prof. En-Hua Yang, Fax: +65 67910676; Email: ehyang@ntu.edu.sg

19

20 **Abstract**

21 In this study, conversion of municipal solid waste incineration bottom ash (IBA) into
22 highly efficient sorbents for Cu(II) removal was reported. The formation of tobermorite
23 induced by humic acid (HA) and IBA under hydrothermal condition was explored and its
24 potential application for efficient removal of Cu(II) ions was further investigated. After
25 hydrothermal treatment, the morphology and microstructure of IBA remarkably changed from
26 sheet-like to particle-like, thereby resulting in substantial increases of sorption capacity. The
27 synthesized tobermorite exhibited a strongly enhanced sorption performance toward Cu(II),
28 which was 270.3 mg g⁻¹ and higher than other reported sorbents. The adsorption behaviors were
29 subsequently examined by isotherm and kinetic studies. Langmuir model was found to describe
30 the adsorption process well, suggesting that the adsorption was chemisorption in nature.
31 Therefore, the hydrothermally synthesized tobermorite may be used as sorbents to remove
32 Cu(II). Conversion of IBA into valuable minerals recovers waste into potential resources and
33 alleviates the needs for ash disposal.

34

35 **Keywords:** Municipal solid waste (MSW); incineration bottom ash (IBA); humic acid;
36 hydrothermal treatment; heavy metals

37

38 **1. Introduction**

39 In recent years, the growing generation of municipal solid waste (MSW) has become a
40 great burden to the society because it raises serious environmental and economic concerns (Bai
41 and Sutanto, 2002). Incineration of MSW is an effective approach to reduce the volume and

42 mass of waste by about 90% and 70%, respectively (Chimenos et al., 1999). It is also an
43 important component of the integral management of MSW to recover energy from waste.
44 Incineration bottom ash (IBA) is the major by-product during the incineration process and
45 accounts for 85-95% of all residues by volume (Luo et al., 2017a). In the USA, most of the
46 IBA is disposed of by landfilling, while in some European and Asian countries about 50% of
47 the IBA is utilized as secondary building materials for road construction and cement production
48 (Hjelmar, 1996). To prolong the lifespan of landfills and to recover waste into resources, it is
49 of great interest to recycle and upgrade IBA.

50 Hydrothermal method is an attractive means to convert wastes into valuable products (Luo
51 et al., 2018). For example, given an appropriate Ca/Al/Si ratio, new mineral phases such as
52 katoite, zeolite and tobermorite can be formed upon hydrothermal treatment using IBA as a
53 starting material (Penilla et al., 2003; Wang et al., 2016). The sources of IBA, activation
54 solution, and reaction temperature and time strongly affect the formation of those secondary
55 mineral phases (Etoh et al., 2009). The main chemical reactions involved in the hydrothermal
56 transformation of IBA inorganic matters are the dissolution of SiO_2 and Al-containing minerals
57 that followed by re-precipitation with Ca-minerals under highly alkaline conditions (Jing et al.,
58 2013). It is well known that IBA also contains a few percentage of organic matters because
59 sometimes they are not completely oxidized by incineration and the partially unburned organic
60 waste materials will co-exist with subsequent formation of new organic compounds (Dugenest
61 et al., 1999).

62 The organic matters in IBA substantially govern the hydrothermal conversion of IBA into
63 different new mineral products and therefore play a crucial role in IBA recycling and utilization.

64 According to the classification of soil organic matter, the organic matters in IBA can be divided
65 into humic substances and non-humic substances. Humic substances are mainly composed of
66 humic acid (HA) and fulvic acid (FA), which have been identified as an important fraction of
67 dissolved organic carbon (DOC) contributing to the complexation of contaminants (Olsson et
68 al., 2007). Besides its presence in IBA, HA has also been found to widely exist in the natural
69 environment and it has a relatively high affinity for binding heavy metals and organic pollutants
70 (Luo et al., 2015). A previous study suggested that HA and FA contributed to 0.3-0.6% and 14-
71 26% of DOC in the leachate from IBA, respectively (Van Zomeren and Comans, 2004). As a
72 typical natural organic matter (NOM), HA can substantially govern the IBA recycling and
73 utilization through binding with heavy metals. Although the role of HA in the hydrothermal
74 conversion of IBA remains unknown, HA would bind heavy metal ions and therefore alter the
75 leaching behavior of IBA.

76 Mostly, IBA is hydrothermally converted into super-porous layered structures or fine
77 particles and crystals, thereby showing excellent adsorption performance due to high specific
78 surface area and ion-exchange capacity (Jing et al., 2007; Wang et al., 2016). The alkaline
79 condition is more favorable to activate the hydrothermal reactions and HA is supposed to
80 participate. The reaction products are subsequently employed as sorbent materials for efficient
81 removal of metal ions and organic dyes from aqueous solution (Wang et al., 2016). Hence,
82 hydrothermal transformation of IBA into sorbent provides a solution to reduce the needs for
83 ash disposal. So far, the HA-involved hydrothermal process of IBA is not well documented and
84 understood. The effect of HA on hydrothermal reaction of IBA and the underlying mechanisms
85 remain unclear.

The main objective of this study is to explore the formation of tobermorite induced by humic acid (HA) and IBA under hydrothermal condition and to further investigate its potential application for efficient removal of Cu(II) ion, a typical hazardous heavy metal in water. The layer-structured IBA was converted into particle-like mineral phases through hydrothermal reaction, thereby showing superior sorption performance toward heavy metals. The chemical, morphological and mineralogical properties of raw IBA and the converted tobermorite were characterized. The adsorption behaviors were subsequently examined by isotherm and kinetic studies. Langmuir model was used to describe the adsorption process, in which chemisorption was determined. Together, these experimental results are of environmental significance because they recover waste into potential resources and alleviate the needs for ash disposal.

2. Materials and methods

2.1. Production, collection and sorting of IBA

MSW-derived IBA samples were obtained from a local Waste-to-Energy (WTE) incineration plant in Singapore, which can treat 800 tons of MSW and generate 2.2×10^7 Watts of green energy every day. According to the data from National Environment Agency (NEA), Singapore, about 7.70 million tons of MSW was generated and 4.72 million tons of MSW was recycled in the year of 2017. The other 2.98 million tons of MSW was disposed and burned consistently without pre-processing at a temperature of 800-1000°C. Waste sources are mainly domestic, including plastics (~25.62%), food waste (~22.71%), paper/cardboard (~19.33%), ash/sludge (~7.21%), textile/leather (~4.74%), horticultural waste (~3.61%), wood (~3.27%),

glass (~1.98%), construction debris (~0.32%), ferrous metal (~0.26%), used slag (~0.10%), scrap tyres (~0.10%), non-ferrous metals (~0.05%), and others (stones, ceramic, rubber, etc., ~10.70%). During incineration, the air-cooled multi-stage grate was the only grate combustion system and the water-cooled multi-stage grate was designed for combustion of higher calorific wastes. To prevent the formation of dust, water was splashed on IBA after the incineration.

IBA can be highly heterogeneous and the properties of IBA may vary with time. To obtain representative IBA samples, 20 kg of fresh IBA was collected once every two weeks from the WTE facility and over a period of five months. After each collection, the fresh IBA was immediately dried in an oven at 105°C for 24 h to remove surface moisture and then sealed to minimize carbonation (Luo et al., 2017a). Altogether, approximate 200 kg of dry IBA was sampled over five months and mixed by a planetary mixer. Prior to use, the 5-month combined IBA was sieved into four size fractions, i.e., < 0.30 mm; 0.30-1.18 mm; 1.18-6.30 mm; and > 6.30 mm. Each size fraction accounts for about 25% of the total weight of IBA. In the current study, < 0.30 mm size fraction was used for subsequent experiments because smaller particles possess higher specific surface area and are more effective for preparation of sorbent materials.

2.2. Hydrothermal synthesis of IBA-based materials

The hydrothermally treated IBA was prepared according to a previous procedure established by the authors (Luo et al., 2017a). The hydrothermally treated (IBA+HA) was synthesized using IBA and humic acid (HA) as the starting materials, no additional Ca, Si and Al elements were introduced. HA was purchased from Sigma-Aldrich Company and was used without further purification. Experiments were performed in a 50 mL Teflon-lined acid

digestion bomb (Parr Instrument Company, USA). The procedures are described as follows:
7.0 g IBA particles were mixed with 35.0 mL reaction solutions, which contained 2.5 M NaOH and different concentrations of HA (10 and 100 ppm, respectively). The mixtures were allowed to stir and react for 30 min at 25°C. The slurry was then transferred into a stainless steel autoclave, carefully sealed and incubated under 180°C for 24 h in the oven. After the hydrothermal reactions, the products were cooled to room temperature and washed three times by repeated centrifugation (5 min at 9000 g, 25°C) using deionized water. The supernatant was discarded and the precipitate was dried in oven at 105°C for 8 h to recover the porous composite material. The mixture of (IBA+HA), which was obtained by mixing 7.0 g IBA with 35.0 mL of 100 ppm HA at pH 7.2 without hydrothermal treatment, was also prepared. The mixture was allowed to react and equilibrate at 25°C on an orbital shaker (SKF-3100, Jeio Tech) under 200 rpm for 24 h. The reaction product was similarly collected as described above. The non-treated IBA (< 0.30 mm) were characterized and tested as control samples.

2.3. Characterizations of the HA and IBA samples before and after hydrothermal treatment

The chemical compositions of the raw IBA were determined using the sequential X-ray fluorescence (XRF) spectrometer (S8 Tiger, Bruker). IBA (< 0.3 mm) samples in loose powder form were analyzed as pressed pellets with the pre-calibrated standard method. Table 1 summarizes the XRF results. As can be seen, IBA used in the current study mainly consists of CaO (54.06%), SiO₂ (8.24%), and Al₂O₃ (6.85%). High amount of CaO in IBA (< 0.3 mm) is due to the presence of Ca-containing solid wastes such as food waste, which easily broke down into smaller particles during incineration. SiO₂ and Al₂O₃ in IBA originate from Si- and Al-

152 containing solid wastes, e.g., glassware and baverage cans, respectivley. Ferrous metals are
153 recovered after incineration through magnetic separation in the incineration plant and thus
154 content of ferrous oxide in IBA is limited.

155 The morphological characteristics of the IBA-based materials were observed by imaging
156 with a field emission scanning electron microscope (FESEM, JSM-7600F, JEOL). The
157 experimental samples were pre-treated by gold coating before the test.

158 The UV-vis spectra of the HA and IBA samples before and after hydrothermal treatment
159 were recorded in the range of 200-800 nm using UV-vis spectrophotometer (UV-2600,
160 Shimadzu). The infrared (IR) spectra of the HA and IBA samples before and after hydrothermal
161 treatment were further characterized in the range of 400-4000 cm^{-1} on a Nicolet iS50 FT-IR
162 spectrometer (Thermo Scientific, USA).

163 Powder X-ray diffraction (XRD) patterns were collected on a Bruker AXS D8 advance
164 diffractometer using Cu K α radiation ($\lambda = 0.154$ nm) with the tube voltage of 40 kV and the
165 current of 40 mA. The XRD diffraction patterns were acquired in the 2θ range of 5-80° at a
166 scan speed of 2° min^{-1} . The phase identification was performed by searching the International
167 Center for Diffraction Data (ICDD) and matching with those included in the Joint Committee
168 on Powder Diffraction Standards (JCPDS) files.

169 Upon the Brunauer-Emmett-Teller (BET) nitrogen adsorption-desorption isotherms, the
170 specific surface area was determined through an automated surface area and pore size analyzer
171 (Quadrasorb evo, Quantachrome Instruments). The pore size distribution was calculated
172 according to the desorption Barrett-Joyner-Halenda (BJH) method. The outgas temperature

was set at 180°C and the outgas time was 18 h. Data analysis was carried out using the QuadraWin software.

2.4. Batch sorption experiments toward Cu(II)

The batch sorption experiments were performed to investigate the sorption kinetics and isotherms of the IBA materials toward Cu(II) in aqueous solution. Cu(II) ion was used in the form of Cu(NO₃)₂. The sorption kinetics were obtained by adding 0.1 g of the IBA samples into 50 mL working solutions with two different initial Cu(II) dosages of 100 and 500 mg g⁻¹. These two concentrations were tested in order to estimate the maximum absorption capacity and the incubation time required to reach the adsorption equilibrium. All assays were prepared in triplicate and error bars were calculated according to the standard deviation of triplicate samples. Control experiments were similarly performed without IBA sorbents. The solution pH was adjusted to 5.0 using 2 wt.% HNO₃ or NaOH. The reaction solutions were stirred and incubated at 25°C over a period of 10 h on the orbital shaker under 250 rpm. At specified time intervals, 1 mL of the reactant was taken and sacrificed to quantify the residual and sorbed concentrations of Cu(II). Prior to analysis, samples were immediately diluted ten times and filtered through 0.2-μm Acrodisc polyethersulfone membrane syringe filters (Pall Corp., Singapore). The concentrations of Cu(II) ion in the solutions were determined using an inductively coupled plasma-mass spectrometer (ICP-MS, ELAN DRC-e, PerkinElmer).

To further obtain the sorption isotherms of Cu(II) onto the IBA materials, batch sorption experiments were conducted using 100 mL shaking flasks, in which 50 mL of Cu(II) working solutions and 0.1 g of different IBA samples were added. The initial Cu(II) concentrations in

the solutions were designed from 50 to 1000 mg L⁻¹. The reactants were mixed together, and subsequently allowed to react and equilibrate at 25°C for 24 h on the orbital shaker under 250 rpm. To prevent the precipitation, the solution pH was adjusted to 5.0. After equilibration, the concentrations of remaining free Cu(II) ions in the solutions were measured and the adsorption amounts of Cu(II) by the IBA materials were calculated.

The adsorption processes of Cu(II) from aqueous solution onto the IBA materials were described by the Langmuir isotherm equation (Luo et al., 2016). Following are the original form (Eq. 1) and a linearized form (Eq. 2) of the Langmuir isotherm:

$$q_e = \frac{bq_{\max}C_e}{1+bC_e} \quad (1)$$

$$\frac{C_e}{q_e} = \frac{C_e}{q_{\max}} + \frac{1}{bq_{\max}} \quad (2)$$

where C_e is the residual Cu(II) concentration at equilibrium (mg L⁻¹); q_e is the amount of Cu(II) adsorbed at equilibrium (mg g⁻¹); q_{\max} is the maximum adsorption capacity of the IBA materials at equilibrium (mg g⁻¹); and b (L mg⁻¹) is the Langmuir constant (Luo et al., 2014; Wang et al., 2016). C_e/q_e and C_e were measured experimentally and q_{\max} can be derived by plotting C_e/q_e in the y-axis against C_e in the x-axis. Linear fitting between C_e/q_e and C_e was then carried out to determine the slope of the line. q_{\max} was calculated by taking the inverse of the slope of the line.

3. Results and discussion

3.1. Morphology of IBA and its composite materials with HA

Fig. 1 shows the morphology of the raw and hydrothermally treated IBAs at different magnifications. The sheet-like microstructures of the raw IBA were relatively solid and dense in Fig. 1a (top row), whereas those of the hydrothermally treated IBA in Fig. 1b (bottom row) were much more porous with aggregation of fine crystals and particles on the surface. As can be seen, the morphology of IBA remarkably changed after the hydrothermal treatment, which was consistent with previous studies (Jing et al., 2010). The morphological changes of IBA could be attributed to the formation of new crystal phases through dissolution of SiO_2 and Al-containing minerals and subsequent re-precipitation with Ca-minerals under highly alkaline conditions (Luo et al., 2017a). As a result, the reaction products might contain zeolite, katoite and gehlenite (Pena et al., 2006).

Fig. 2 shows the morphology of the composite materials synthesized by IBA and HA. The IBA-HA complex in Fig. 2a (top row) was obtained without hydrothermal treatment and its morphology exhibited the layered structures with aggregation of solid and dense sheets, which was similar to that of the raw IBA in Fig. 1a. The microstructures of the composite material that combined with IBA and 10 ppm HA after hydrothermal treatment were presented in Fig. 2b (middle row). As can be seen, a mixture of the smooth sheets and fine particles was observed in Fig. 2b, suggesting HA was able to promote the morphological transformation of IBA from sheets to particles. This could be confirmed by further analysis of Fig. 2c (bottom row), in which another composite material that combined with IBA and 100 ppm HA mainly consisted of fine particles after hydrothermal treatment. Thus, the increased dosage of HA resulted in the formation of more fine particles under hydrothermal conditions. The hydrothermally treated IBA without HA addition in Fig. 1b also provided evidence to support this conclusion. A

possible explanation for the effect of HA was that the addition of HA would contribute to the dissolution of IBA in the presence of alkali by complexing with the metal ions and therefore effectively prevent the deposition of altered mineral phases on the surface of original IBA samples.

3.2. Spectroscopic characterizations of HA, IBA and their composite materials

Fig. 3 shows the UV-vis spectra of different species including HA, IBA and their composite materials. As can be seen, the spectra of IBA samples exhibited a continuous decrease with a broad peak for the raw IBA around 252 nm and a sharp crest for the hydrothermally treated IBA at 262 nm. The absorbance of the treated IBA in Fig. 3 decreased much faster than that of the raw IBA, especially at wavelength longer than 262 nm. The UV-vis spectrum of HA was broad, featureless and monotonously decreased with an increasing wavelength (Luo et al., 2017b). The observed differences in the patterns of UV-vis absorption might be attributed to the formation of different mineral crystal structures after hydrothermal treatment and the presence of various organic matters in IBA materials (Luo et al., 2017a).

Fig. 4 shows the FT-IR spectra of HA, IBA and their composite materials. As can be seen, similar patterns were found at larger wavenumbers and the differences in absorption bands were mainly observed between 500-1500 cm^{-1} for IBA samples, which could be attributed to the asymmetric and symmetric stretching vibrations of Si-O, Al-O or Si-O-Al bonds (Bai et al., 2008; Penilla et al., 2003). According to previous studies, the intense peaks at 1407, 871 and 712 cm^{-1} were associated with the presence of CaCO_3 (Legodi et al., 2001), while the O-H stretching vibration in Ca(OH)_2 occurred at 3633 cm^{-1} (Reig et al., 2002). After hydrothermal

treatment with and without HA, all those peaks either disappeared or markedly diminished. At the same time, a new band was present at 957 cm^{-1} typically for treated IBA, indicating the hydrothermal reactions likely produced new mineral structures containing Ca, Al and Si (Jing et al., 2013).

As for HA, the broad band at 3300 cm^{-1} was assigned to H-bonded OH group. The two peaks occurring at 2919 and 2849 cm^{-1} were attributed to the asymmetric and symmetric aliphatic C-H stretching of CH_2 group. The weak peak at 1729 cm^{-1} was caused by C=O stretching of COOH group, while another weak band at 1631 cm^{-1} was attributed to the aromatic C=C skeletal vibrations and C=O stretching of quinones. The intense peak at 1557 cm^{-1} belonged to the aromatic C=C stretching. The obvious band at 1367 cm^{-1} was assigned to the C-H deformation of CH_2 and CH_3 groups and/or to the antisymmetric stretching of COO^- group (Luo et al., 2015; Wu et al., 2016).

3.3. Mineralogical analysis of IBA and its composite materials with HA

Fig. 5 shows the XRD diffractograms of IBA and its composite materials with HA before and after hydrothermal treatment. As can be seen, the crystal phases in raw IBA ($< 0.3\text{ mm}$) were mainly Ca-bearing minerals such as calcite (CaCO_3 , 29.47°) and portlandite (Ca(OH)_2 , 47.56° and 48.56°). The diffraction peak of quartz (SiO_2 , 26.64°) was not typically observed in raw IBA with size less than 0.3 mm . This finding was in accordance with the analysis of Table 1 and could be further explained by the fact that IBA particles less than 0.3 mm have the highest content of Ca and lowest content of Si than other size fractions. The IBA-HA complex showed a similar XRD pattern as the raw IBA since no hydrothermal reaction took place and the major

mineral phases remained unchanged. However, the composite materials, especially after hydrothermal treatment with 100 ppm HA, exhibited many new characteristic peaks at 2θ of 23.16° , 31.68° , 32.88° , 36.04° , 39.56° and 43.28° , indicating hydrothermal reactions of IBA with HA simultaneously changed the morphology and mineralogy of IBA particles. After matched with JCPDS files and compared with related literatures, the newly formed crystal phases were identified as tobermorite (JCPDS card No. 45-1480 and JCPDS card No. 19-1364) (Jing et al., 2007). Moreover, the use of 100 ppm HA resulted in the highest yield of tobermorite during synthesis of the composite materials considering the intensity of diffraction peak. While many factors may affect the formation of tobermorite, the mole ratio of Ca/Si/Al in IBA is the most important factor. Thus, tobermorite can be synthesized via a suitable pathway using IBA as starting material, as long as an appropriate ratio of Ca/Si/Al is given. Coincided with above FT-IR analysis, the original crystal phases became minor ones or even disappeared and meanwhile new crystal phases were evidently formed after treatment, suggesting an excellent efficiency of hydrothermal conversion for raw IBA. Note that, secondary crystal phases such as gehlenite, katoite and zeolite were not typically found in current study, probably due to different molar ratios of Ca/Al/Si in raw IBA that collected from different sources.

3.4. The BET surface property of IBA and its composite materials with HA

The results of BET tests are shown in Fig. 6. As can be seen, an increase in N_2 adsorption capacity of IBA was observed after hydrothermal treatment, regardless of the presence of HA. The calculated BET surface area was $26.9 \text{ m}^2 \text{ g}^{-1}$ for the treated (IBA+HA) and $23.1 \text{ m}^2 \text{ g}^{-1}$ for the IBA-HA complex (Fig. 6a), and was $20.5 \text{ m}^2 \text{ g}^{-1}$ for treated IBA and $17.9 \text{ m}^2 \text{ g}^{-1}$ for raw

IBA (Fig. 6b). The high surface area suggests the evolution of porosity and potential for pollutants removal. As per the instructions from IUPAC, the N₂ sorption isotherms were classified as type IV with a hysteresis loop of type H3 (Thommes et al., 2015). The presence of the hysteresis loop at high relative pressure indicated the mesoporous structure in IBA, whereas the sorption capacity of N₂ was attributed to the micropores at low relative pressure (Figs. 6a and b). The pore volume is indicative of total porosity (cm³ g⁻¹), and further analysis of the cumulative pore volume as a function of pore radius showed that the pore volume of modified IBA increased faster than that of raw IBA, especially at a larger pore radius (Fig. 6c). The differential pore size distribution of IBA was obtained by the Desorption Barrett-Joyner-Halenda (BJH) method (Fig. 6d). The intensity of the sharp peak in Fig. 6d indicates the mesopores with an average radius of 20.2 ± 0.1 Å existed in the IBA materials, and the amount of mesopores increased after hydrothermal treatment. Thus, the hydrothermal treatment may have changed the porosity, the pore structure, and the adsorption capacity of IBA because the reactions can form new mineral materials.

3.5. Sorption kinetics and isotherms of Cu(II) from aqueous solution

Fig. S1 shows the sorption kinetics of Cu(II) onto IBA and its composite materials at pH 5.0 under different initial dosages. As can be seen, the adsorption equilibrium was rapidly reached within 2 h of incubation. Meanwhile, over 95% of Cu(II) was removed by the IBA-based materials when 100 mg g⁻¹ of Cu(II) was added (Fig. S1a). In contrast, the removal ratio decreased to 35%-50% when 500 mg g⁻¹ of Cu(II) was introduced and the adsorption equilibrium was achieved almost after reaction for 8 h (Fig. S1b). The Cu(II) absorption

capacities within 10 h in Fig. S1b were ranging from approximately 175 to 250 mg g⁻¹ as treated by different IBA sorbents. It was also found that the composite material, i.e., the HA-induced tobermorite exhibited the fastest removal rate of Cu(II) than other sorbent materials such as raw IBA, the treated IBA and IBA-HA complex. The IBA-HA complex was observed to possess the higher Cu(II) absorption capacity than the treated IBA probably because without hydrothermal conditions, a small fraction of HA could bind or sorb onto the surface of IBA due to its carboxyl and hydroxyl groups, and thus contribute to Cu(II) absorption. Overall, the IBA particles after hydrothermal treatment would be composed of various new mineral phases, possessing higher specific surface area and macro- and mesoporous structures (Chiang et al., 2014; Wang et al., 2016). In this study, the addition of HA further induced the formation of tobermorite and improved its surface properties upon hydrothermal treatment with IBA, thereby resulting in a superior sorption performance toward Cu(II) ions from aqueous solution. Control experiments showed that no sorption occurred on either glassware or filtration systems. Consequently, the observed Cu(II) removal was attributed to the adsorption by IBA materials.

The maximum adsorption capacity of IBA materials toward Cu(II) was determined using the Langmuir model. Fig. S2 shows the adsorption data of Cu(II), which can be fitted well into a linearized form of Langmuir isotherm equation (Eq. 2) with the correlation factor of $R^2 > 0.98$. This indicated that the adsorption of Cu(II) ions onto the surface sites of sorbents could be modeled by monolayer adsorption and the adsorption process was thermodynamically favorable. Analysis of the data in Fig. S2 further revealed that the maximum adsorption capacity toward Cu(II) was 147.06±8.25 mg g⁻¹ for the raw IBA (Fig. S2a), 178.57±6.96 mg g⁻¹ for the treated IBA (Fig. S2b), 212.77±11.36 mg g⁻¹ for the IBA-HA complex (Fig. S2c), and

270.27±16.44 mg g⁻¹ for the treated (IBA+HA) (Fig. S2d). The Langmuir constant (*b*) was calculated according to the linearized isotherm equation, which was 0.048, 0.028, 0.011, and 0.005 L mg⁻¹, respectively. Compared to previous investigations (Chiang et al., 2012; Wang et al., 2016), raw IBA in current study showed a relatively high adsorption capacity because smaller particles were used and higher specific surface area was available. The hydrothermal treatment of IBA, especially with the presence of HA led to a better sorption performance toward Cu(II) due to the HA-induced formation of tobermorite. The comparison of Cu(II) sorption capacity by IBAs and other sorbents is presented in Table 2. As a low-cost waste material, the IBA particles were much more effective in removing Cu(II) than other sorbents such as activated carbon (Demiral and Güngör, 2016), granular sludge (Luo et al., 2014), chitosan (Ngah and Fatinathan, 2008), biochar (Pellera et al., 2012), zeolite (Wang et al., 2008), bentonite (Veli and Alyuz, 2007), goethite (Weng et al., 2008), and cellulose (Shen et al., 2009). These results suggested that IBA, especially after hydrothermal treatment with HA, was a promising sorbent to efficiently remove Cu(II) ions. While the effort to be paid for hydrothermal as proposed in the current study can be high, it may be offset by other factors. For example, in land scarce city, such as Singapore, IBA recycling not only prolongs the lifespan of landfills but also create alternative local resources from wastes. Other tangible and intangible benefits include alleviating the disposal costs of the ash, preserving land capacity, conserving dwindling supplies of natural raw materials, and mitigating potential environmental impacts. In this circumstance, IBA recycling is not only driven by economic sense and government may provide incentives to encourage IBA usage. Further studies, e.g., the leaching

behavior and the life cycle (cost) assessment, are necessary before practical adoption of the current approach.

4. Conclusions

In this study, the formation of tobermorite induced by humic acid and municipal solid waste incineration bottom ash upon hydrothermal treatment was reported and its potential application for efficient removal of Cu(II) ions was further investigated. Experimental results showed that the morphology and microstructure of IBA remarkably changed from sheet-like to particle-like after hydrothermal treatment, thereby resulting in substantial increases of sorption capacity and specific surface area. The synthesized tobermorite exhibited a strongly enhanced sorption performance toward Cu(II), which was 270.3 mg g⁻¹ and higher than other reported sorbents. The adsorption behaviors were examined by isotherm and kinetic studies. Langmuir model was found to describe the adsorption process well, suggesting that the adsorption was chemisorption in nature. Considering the very good results obtained for Cu(II), future studies can be addressed to evaluate the sorption capacity of the composite material with other heavy metals. In that case, the hydrothermally synthesized tobermorite may be used as sorbents to remove various heavy metals. Conversion of IBA into valuable minerals recovers waste into potential resources and alleviates the needs for ash disposal.

Acknowledgements

The authors gratefully acknowledge financial supports from the Environment Technology Research Program (ETRP), National Environment Agency, Singapore (ETRP 1301 104),

National Science Foundation of China (No. 21806140) and Start-Up Grant from Zhejiang University of Technology (No. 2017129004429). Dr. Bin Cao is gratefully acknowledged for contributing several chemicals and for helpful discussion.

References

- Bai, J., Li, W., Li, B.Q., 2008. Characterization of low-temperature coal ash behaviors at high temperatures under reducing atmosphere. *Fuel* 87, 583-591.
- Bai, R.B., Sutanto, M., 2002. The practice and challenges of solid waste management in Singapore. *Waste Manage.* 22, 557-567.
- Chiang, Y.W., Ghyselbrecht, K., Santos, R.M., Meesschaert, B., Martens, J.A., 2012. Synthesis of zeolitic-type adsorbent material from municipal solid waste incinerator bottom ash and its application in heavy metal adsorption. *Catal. Today* 190, 23-30.
- Chiang, Y.W., Santos, R.M., Vanduyfhuys, K., Meesschaert, B., Martens, J.A., 2014. Atom-efficient route for converting incineration ashes into heavy metal sorbents. *ChemSusChem* 7, 276-283.
- Chimenos, J.M., Segarra, M., Fernandez, M., Espiell, F., 1999. Characterization of the bottom ash in municipal solid waste incinerator. *J. Hazard. Mater.* 64, 211-222.
- Demiral, H., Güngör, C., 2016. Adsorption of copper(II) from aqueous solutions on activated carbon prepared from grape bagasse. *J. Clean. Prod.* 124, 103-113.
- Dugenest, S., Combrisson, J., Casabianca, H., Grenier-Loustalot, M.F., 1999. Municipal solid waste incineration bottom ash: Characterization and kinetic studies of organic matter. *Environ. Sci. Technol.* 33, 1110-1115.

413 Etoh, J., Kawagoe, T., Shimaoka, T., Watanabe, K., 2009. Hydrothermal treatment of MSWI
 414 bottom ash forming acid-resistant material. *Waste Manage.* 29, 1048-1057.

415 Hjelmar, O., 1996. Disposal strategies for municipal solid waste incineration residues. *J.*
 416 *Hazard. Mater.* 47, 345-368.

417 Jing, Z.Z., Fan, X.W., Zhou, L., Fan, J.J., Zhang, Y., Pan, X.H., Ishida, E.H., 2013.
 418 Hydrothermal solidification behavior of municipal solid waste incineration bottom ash
 419 without any additives. *Waste Manage.* 33, 1182-1189.

420 Jing, Z.Z., Jin, F.M., Yamasaki, N., Ishida, E.H., 2007. Hydrothermal synthesis of a novel
 421 tobermorite-based porous material from municipal incineration bottom ash. *Ind. Eng.*
 422 *Chem. Res.* 46, 2657-2660.

423 Jing, Z.Z., Ran, X.Q., Jin, F.M., Ishida, E.H., 2010. Hydrothermal solidification of municipal
 424 solid waste incineration bottom ash with slag addition. *Waste Manage.* 30, 1521-1527.

425 Legodi, M.A., de Waal, D., Potgieter, J.H., Potgieter, S.S., 2001. Rapid determination of CaCO_3
 426 in mixtures utilising FT-IR spectroscopy. *Miner. Eng.* 14, 1107-1111.

427 Luo, H.W., Law, W.W., Wu, Y.C., Zhu, W.P., Yang, E.H., 2018. Hydrothermal synthesis of
 428 needle-like nanocrystalline zeolites from metakaolin and their applications for efficient
 429 removal of organic pollutants and heavy metals. *Micropor. Mesopor. Mat.* 272, 8-15.

430 Luo, H.W., Chen, J.J., Sheng, G.P., Su, J.H., Wei, S.Q., Yu, H.Q., 2014. Experimental and
 431 theoretical approaches for the surface interaction between copper and activated sludge
 432 microorganisms at molecular scale. *Sci. Rep.* 4, 7078.

433 Luo, H.W., Lin, Z.Q., Sheng, G.P., 2015. Spectroscopic characterization of the complexes
 434 between Fe/Mn and natural organic matters by electron paramagnetic resonance and

435 synchrotron-based techniques. *Ecotoxicology* 24, 2207-2212.

436 Luo, H.W., Wang, L.F., Tong, Z.H., Yu, H.Q., Sheng, G.P., 2016. Approaching the binding
 437 between Cu(II) and aerobic granules by a modified titration and μ -XRF. *Front. Env. Sci.*
 438 *Eng.* 10, 362-367.

439 Luo, H.W., Wu, Y.C., Zhao, A.Q., Kumar, A., Liu, Y.Q., Cao, B., Yang, E.H., 2017a.
 440 Hydrothermally synthesized porous materials from municipal solid waste incineration
 441 bottom ash and their interfacial interactions with chloroaromatic compounds. *J. Clean.*
 442 *Prod.* 162, 411-419.

443 Luo, H.W., Yin, X.P., Jubb, A.M., Chen, H.M., Lu, X., Zhang, W.H., Lin, H., Yu, H.Q., Liang,
 444 L.Y., Sheng, G.P., Gu, B.H., 2017b. Photochemical reactions between mercury (Hg) and
 445 dissolved organic matter decrease Hg bioavailability and methylation. *Environ. Pollut.*
 446 220, 1359-1365.

447 Ngah, W.S.W., Fatinathan, S., 2008. Adsorption of Cu(II) ions in aqueous solution using
 448 chitosan beads, chitosan-GLA beads and chitosan-alginate beads. *Chem. Eng. J.* 143, 62-
 449 72.

450 Olsson, S., Van Schaik, J.W.J., Gustafsson, J.P., Kleja, D.B., Van Hees, P.A.W., 2007. Copper(II)
 451 binding to dissolved organic matter fractions in municipal solid waste incinerator bottom
 452 ash leachate. *Environ. Sci. Technol.* 41, 4286-4291.

453 Pelleri, F.M., Giannis, A., Kalderis, D., Anastasiadou, K., Stegmann, R., Wang, J.Y., Gidarakos,
 454 E., 2012. Adsorption of Cu(II) ions from aqueous solutions on biochars prepared from
 455 agricultural by-products. *J. Environ. Manage.* 96, 35-42.

456 Pena, R., Guerrero, A., Goni, S., 2006. Hydrothermal treatment of bottom ash from the

457 incineration of municipal solid waste: Retention of Cs(I), Cd(II), Pb(II) and Cr(III). J.
 458 Hazard. Mater. 129, 151-157.

459 Penilla, R.P., Bustos, A.G., Elizalde, S.G., 2003. Zeolite synthesized by alkaline hydrothermal
 460 treatment of bottom ash from combustion of municipal solid wastes. J. Am. Ceram. Soc.
 461 86, 1527-1533.

462 Reig, F.B., Adelantado, J.V.G., Moreno, M.C.M.M., 2002. FTIR quantitative analysis of
 463 calcium carbonate (calcite) and silica (quartz) mixtures using the constant ratio method.
 464 Application to geological samples. Talanta 58, 811-821.

465 Shen, W., Chen, S., Shi, S., Li, X., Zhang, X., Hu, W., Wang, H., 2009. Adsorption of Cu(II)
 466 and Pb(II) onto diethylenetriamine-bacterial cellulose. Carbohydr. Polym. 75, 110-114.

467 Thommes, M., Kaneko, K., Neimark, A.V., Olivier, J.P., Rodriguez-Reinoso, F., Rouquerol, J.,
 468 Sing, K.S.W., 2015. Physisorption of gases, with special reference to the evaluation of
 469 surface area and pore size distribution (IUPAC Technical Report). Pure Appl. Chem. 87,
 470 1051-1069.

471 Van Zomeren, A., Comans, R.N.J., 2004. Contribution of natural organic matter to copper
 472 leaching from municipal solid waste incinerator bottom ash. Environ. Sci. Technol. 38,
 473 3927-3932.

474 Veli, S., Alyuz, B., 2007. Adsorption of copper and zinc from aqueous solutions by using
 475 natural clay. J. Hazard. Mater. 149, 226-233.

476 Wang, S., Terdkiatburana, T., Tade, M.O., 2008. Adsorption of Cu(II), Pb(II) and humic acid
 477 on natural zeolite tuff in single and binary systems. Sep. Purif. Technol. 62, 64-70.

478 Wang, Y.B., Huang, L., Lau, R., 2016. Conversion of municipal solid waste incineration bottom

479 ash to sorbent material for pollutants removal from water. J. Taiwan Inst. Chem. E 60,
480 275-286.

481 Weng, L., Van Riemsdijk, W.H., Hiemstra, T., 2008. Cu²⁺ and Ca²⁺ adsorption to goethite in
482 the presence of fulvic acids. Geochim. Cosmochim. Acta 72, 5857-5870.

483 Wu, M., Song, M.Y., Liu, M., Jiang, C.Y., Li, Z.P., 2016. Fungicidal activities of soil
484 humic/fulvic acids as related to their chemical structures in greenhouse vegetable fields
485 with cultivation chronosequence. Sci. Rep. 6, 32858.

Table 1 Chemical compositions of incineration bottom ash (IBA) used in the current study.

Component	Content (wt.%)
CaO	54.06
SiO ₂	8.24
SO ₃	7.89
Al ₂ O ₃	6.85
P ₂ O ₅	4.83
Fe ₂ O ₃	4.59
Cl	3.69
Na ₂ O	2.55
MgO	2.38
TiO ₂	1.75
K ₂ O	1.37
ZnO	0.79
CuO	0.25
BaO	0.24
MnO	0.16
PbO	0.10
Cr ₂ O ₃	0.08
SrO	0.07
SnO ₂	0.05
NiO	0.02
ZrO ₂	0.02
Total	99.98

Table 2 Comparison of Cu(II) sorption capacity by IBAs and other sorbents.

Sorbents	Cu(II) sorbed (mg g ⁻¹)	Reference
Raw IBA	147.06	This study
Treated IBA	178.57	This study
IBA-HA complex	212.77	This study
Treated (IBA+HA)	270.27	This study
Activated carbon	37.17	Demiral et al., 2016
Granular sludge	25.70	Luo et al., 2014
Chitosan	64.62	Ngah et al., 2008
Biochar	10.26	Pellera et al., 2012
Zeolite	23.30	Wang et al., 2008
Bentonite	44.84	Veli et al., 2007
Goethite	10.70	Weng et al., 2008
Cellulose	63.09	Shen et al., 2009

Figure Captions

Fig. 1. Morphology of (a) the raw IBA (top row); and (b) the corresponding hydrothermally treated IBA (bottom row).

Fig. 2. Morphology of (a) IBA mixed with HA before hydrothermal treatment (top row); (b) IBA mixed with 10 ppm HA after hydrothermal treatment (middle row); and (c) IBA mixed with 100 ppm HA after hydrothermal treatment (bottom row).

Fig. 3. UV-vis spectra of different species including HA sample, the raw and the hydrothermally treated IBA, and the IBA mixed with 100 ppm HA after hydrothermal treatment.

Fig. 4. FT-IR spectra of HA sample, the raw and the hydrothermally treated IBA, and the IBA mixed with 100 ppm HA after hydrothermal treatment.

Fig. 5. XRD diffractograms of the IBA samples mixed with and without different concentrations of HA before and after hydrothermal treatment. HA samples with 10 ppm and 100 ppm are used.

Fig. 6. N₂ adsorption-desorption isotherms of (a) IBA mixed with HA before and after hydrothermal treatment and (b) IBA with and without hydrothermal treatment at -196°C; (c) cumulative pore volume and (d) desorption BJH pore size distribution of IBA materials.

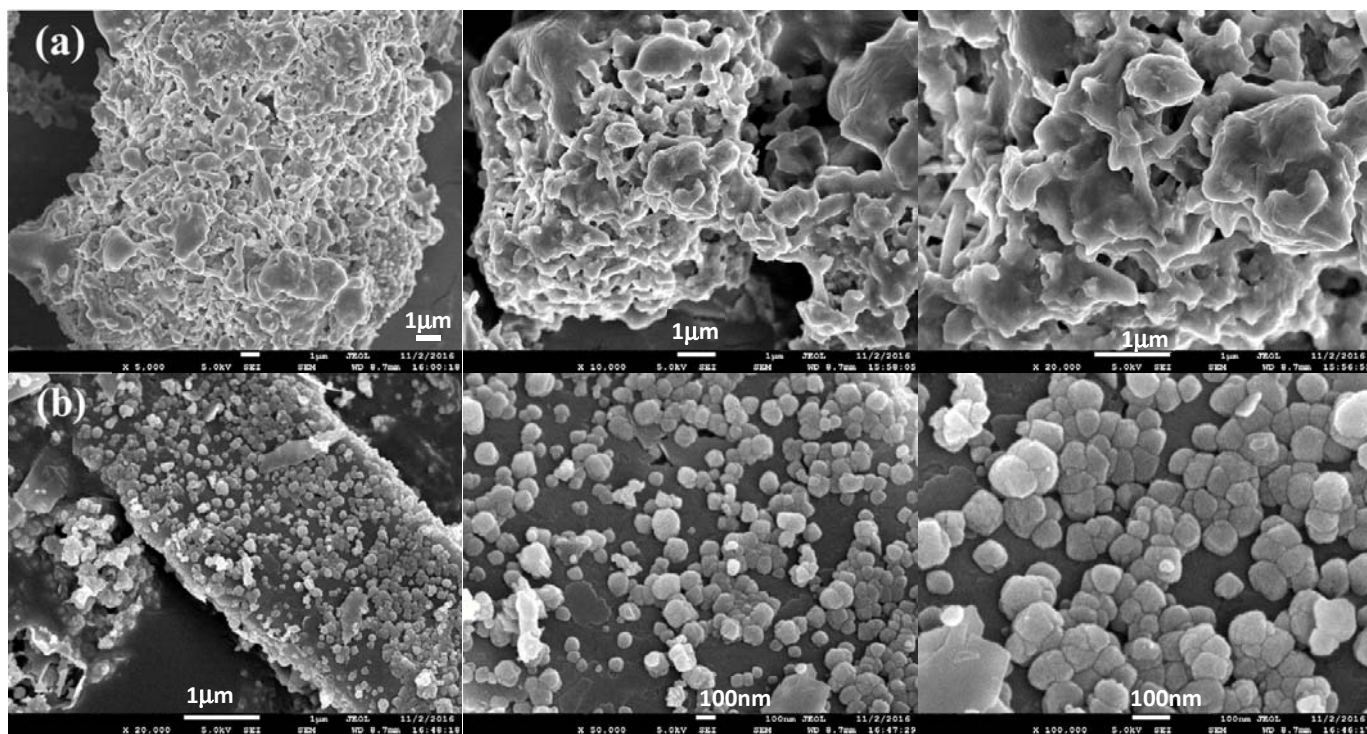


Fig. 1

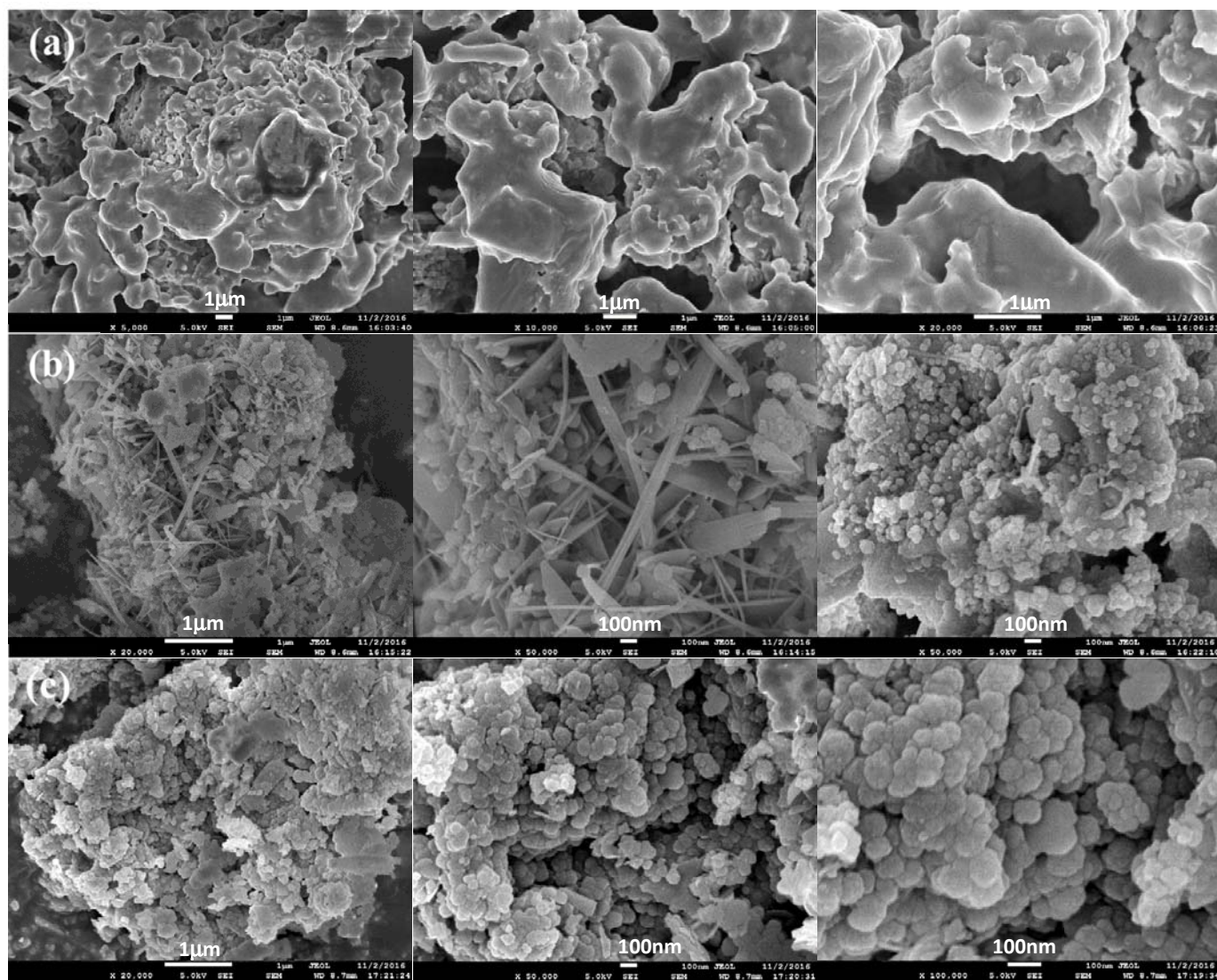


Fig. 2

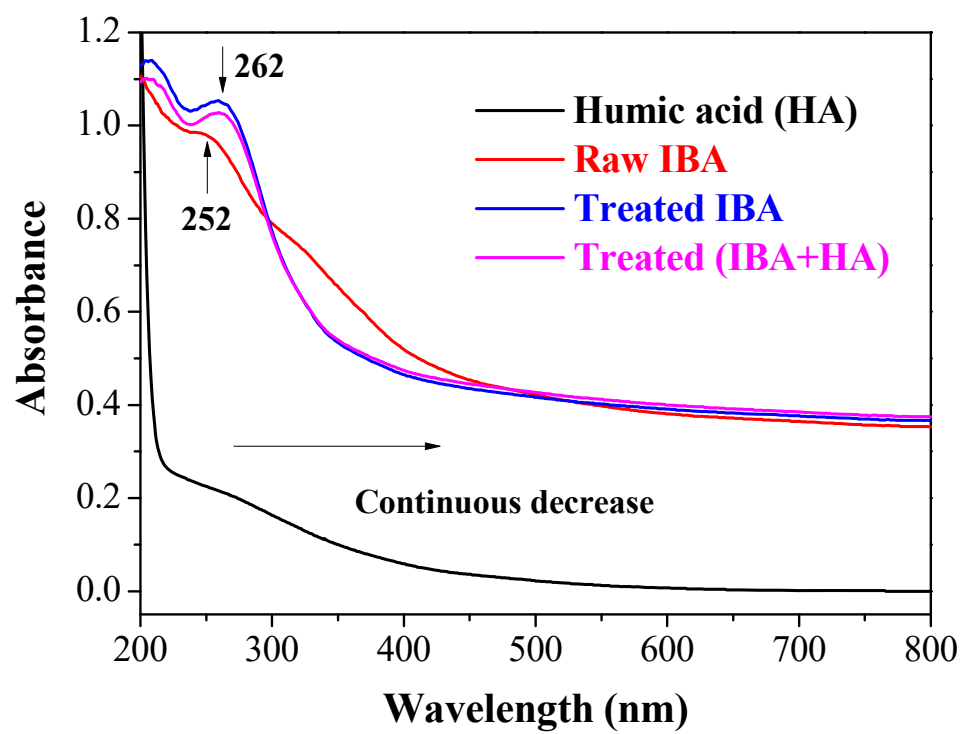


Fig. 3

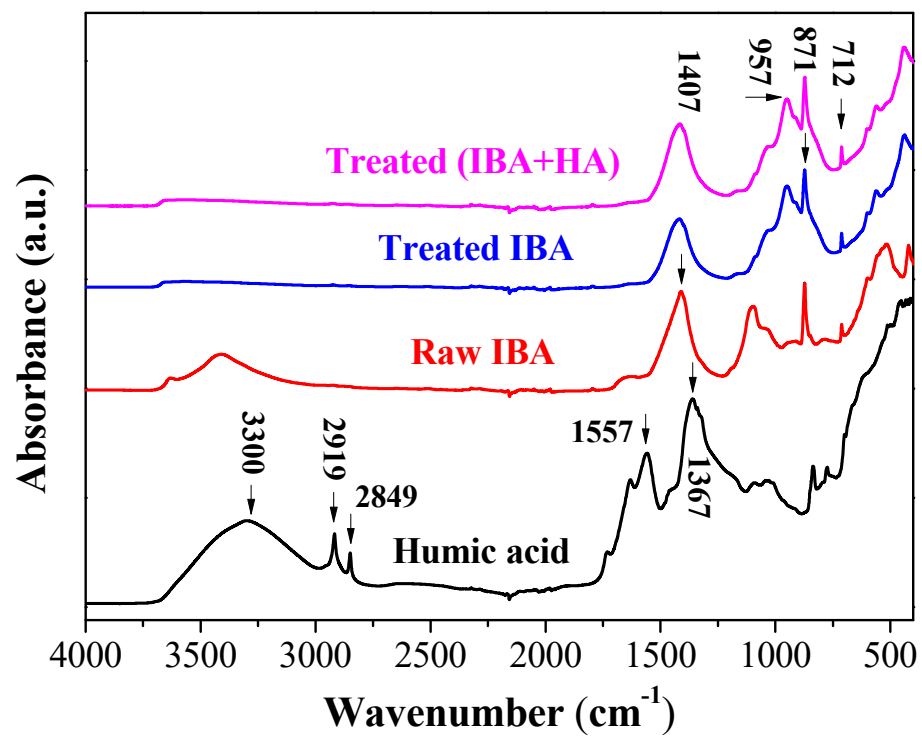


Fig. 4

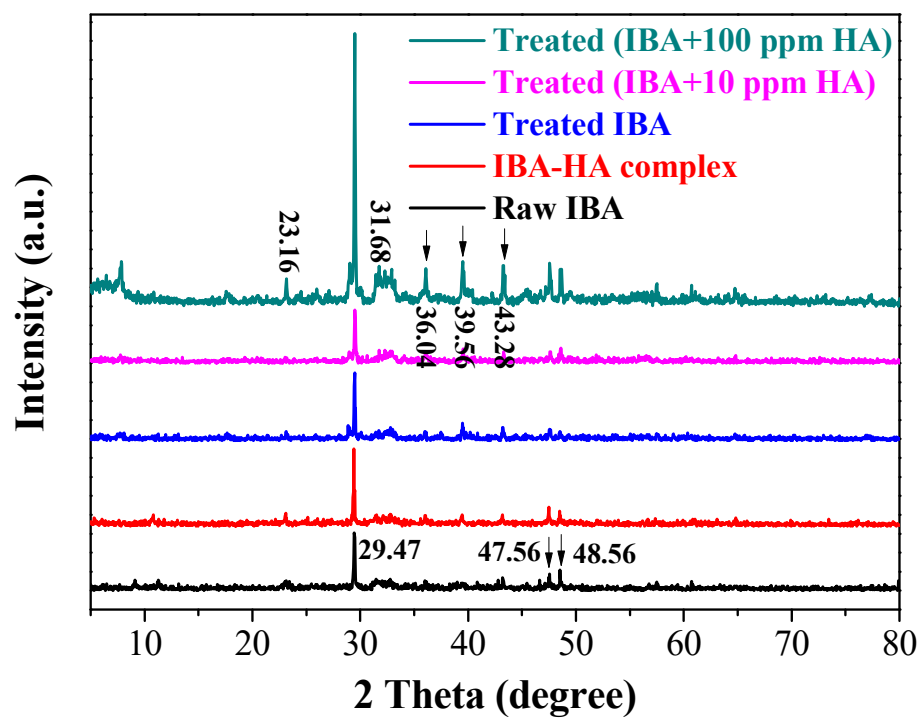


Fig. 5

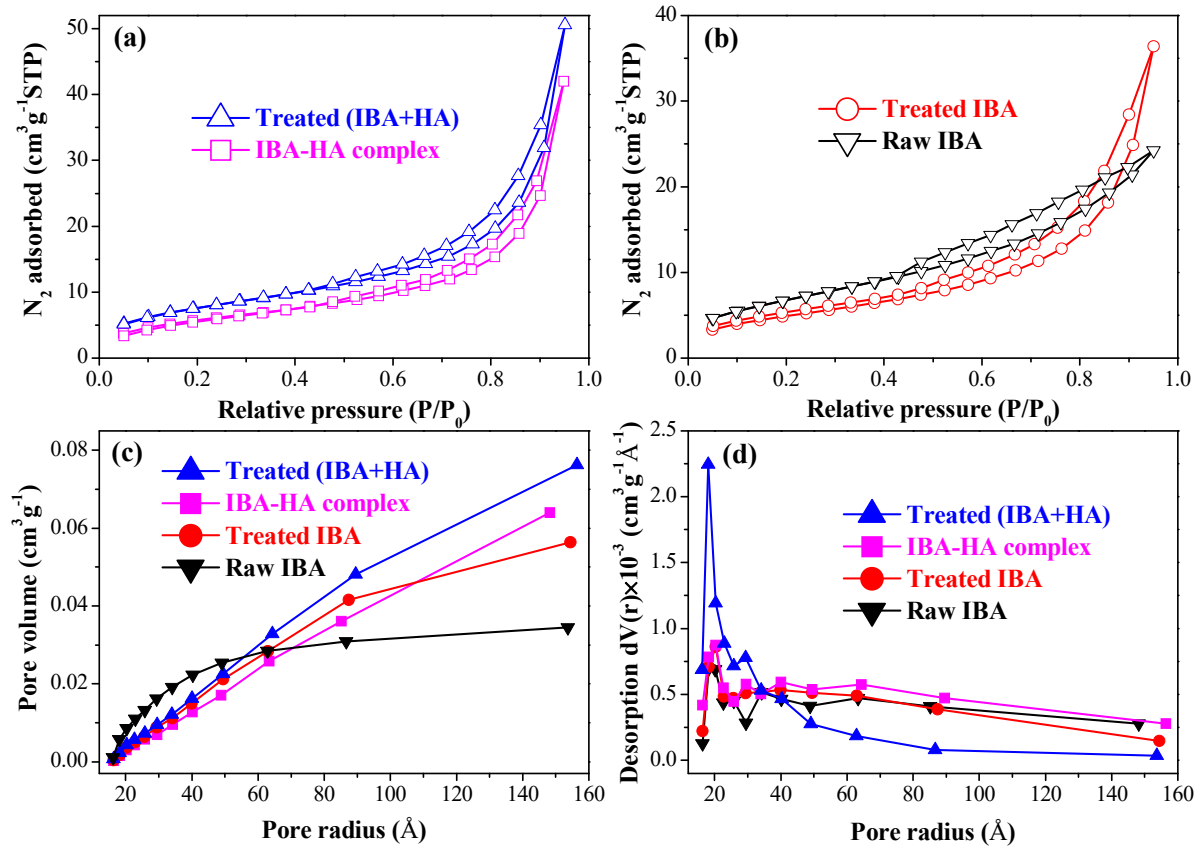


Fig. 6